Numerical simulations of the ice flow dynamics of the Brunt Ice Shelf - Stancomb Wills Ice Tongue System

Angelika Humbert[1], Hamish D. Pritchard[2]

[1]*Section Mechanics, Department of Mechanical Engineering, Darmstadt University of Technology, Hochschulstraße 1,D-64289 Darmstadt, Germany*
humbert@mechanik.tu-darmstadt.de

[2]*British Antarctic Survey, High Cross, Madingley Road, Cambridge, CB3 0ET, UK*

Abstract

Ice shelves play an important role in determining regional ocean properties and in modulating ice flux from land to sea. Their dynamics are complex, however, and localised rifts and zones of weakness can have a significant but poorly understood effect on flow and ultimately on the integrity of the shelf.
The Brunt Ice Shelf (BIS)- Stancomb Wills Ice Tongue (SWIT) System, situated on the Caird Coast, Oates Land, Antarctica, is characterised as a thin, unbounded ice shelf with a highly heterogeneous structure. In contrast to most ice shelves, icebergs calve along much of the grounding line but are trapped and subsequently bound together by sea ice. This calf-ice / sea-ice aggregate makes up a large part of the Brunt Ice Shelf in particular, and this heterogeneity makes the BIS-SWIT a good test case for investigating the importance of weak zones in shelf dynamics.
We applied a diagnostic, dynamic/thermodynamic ice-shelf model to simulate the present flow of the ice shelf that results from the ice-thickness distribution, the influx at the grounding line and the surface and bottom temperature. We then compared the model results with flow velocities measured by Synthetic Aperture Radar feature tracking. We found that our simulations were clearly improved by the use of a high- resolution ice thickness distribution on the heterogeneous ice shelf calculated from ICESat surface elevation data using an assumption of hydrostatic equilibrium. We then assessed the model's sensitivity to ice thickness, inflow velocities and a flow enhancement factor that parameterises the role of sea ice, whose mechanical properties are known to be significantly different from those of meteoric ice.
We found that the numerical simulations were improved by incorporating the detailed variations in shelf structure. Simulated flow velocities on either side of rifts in the ice shelf became decoupled as we softened the sea ice within the rifts. On a larger scale, we found that soft sea ice can lead to a decoupling of the movement of the Stancomb-Wills Ice Tongue and the Brunt Ice Shelf. When we simulated a regime where sea ice was absent, ice shelf flow speeds increased along the western edge of the SWIT ice front, in general agreement with observations made in just such a sea- ice-free dynamic regime that occurred in 1969.

1 Introduction

Ice shelves play an important role in regional ocean circulation through their modifying effects on sub-shelf water properties (Orsi et al., 1999). They can also retard the drainage of their grounded tributary glaciers and so modulate ice sheet volume (Rott et al., 1996; Scambos et al., 2004; Rignot et al., 2004, 2005). However, their viability can be critically sensitive to changes in their stress distribution. Weakening of the shelf through thinning or fracturing can mean that grounded ice rises change in their effect from acting to support the shelf mechanically and retard flow, to acting as indenting wedges that break the shelf apart (Doake and Vaughan, 1991). Also, retreat of a shelf front beyond an arch of compression in the stress field can trigger irreversible shelf collapse (Doake et al., 1998).

Ice shelf flow and calving at the front are both functions of the strength and integrity of the ice shelf and in particular the presence of rifts. In order to understand and predict the behaviour of ice shelves, an approach to dynamic modelling that explicitly incorporates heterogeneity in the detailed shelf structure is therefore needed. Two new remote sensing datasets and techniques, laser altimetry from the GLAS sensor on ICESat and orbit-controlled feature tracking from the ENVISat ASAR sensor, can now provide us with the required high-precision, spatially extensive measurements of ice shelf thickness and flow.

2 The Brunt Ice Shelf / Stancomb-Wills Ice Tongue System

The Brunt Ice Shelf (23.02 to 27.50°W and 75.06 to 76.04°S) flows from the Caird Coast, Coats Land, East Antarctica, into the Weddell Sea (Fig. 1). It has a relatively long record of shelf flow and extent and its dynamics are of particular interest because of the presence on the shelf of the permanently staffed UK research station, Halley (1956 to present). The velocity at the station is now continuously monitored by GPS.

The Brunt Ice Shelf (BIS) and the more easterly Riiser-Larsen Ice Shelf flank the 250 km long Stancomb-Wills Ice Tongue (SWIT), the floating extension of the Stancomb-Wills Ice Stream that crosses the Caird Coast with a velocity of approximately 1200 ma^{-1}(Fig. 1, Gray and Short (2001)). This ice tongue consists of relatively thick (Fig. 2), fast-flowing ice and is separated from the Riiser-Larsen shelf at the ice front by the substantial, 100 km-long Lyddan Ice Rise (Fig. 1).

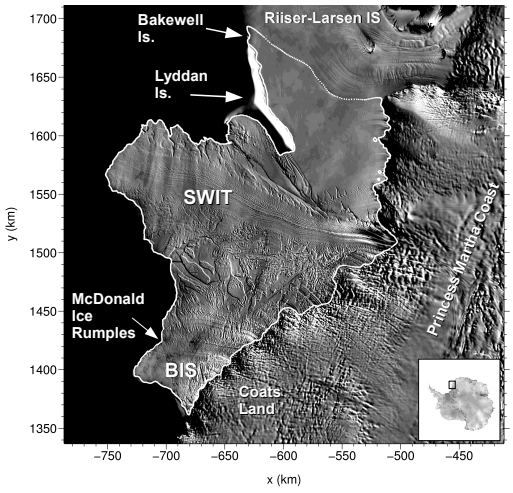

Figure 1: MOA image of the BIS-SWIT (courtesy of Ted Scambos, NSIDC) showing the modelling domain of the Brunt Ice Shelf (BIS) and the Stancomb-Wills Ice Tongue (SWIT), as well as the grounded areas McDonald Ice Rumples, Lyddan Island, Bakewell Island and three nameless ice rises.

The BIS is characterized as a thin, unbounded ice shelf. Both the BIS and the BIS- SWIT shear zone between the fast, thick ice of the tongue and the thinner, slower shelf ice are unusually heterogeneous. They are made up of a discontinuous mass of ice blocks that have calved at the grounding line and, over time, are frozen together by a semi-consolidated melange of sea ice, small bergs and accumulated snow. The ice shelf in this region is therefore formed of thick meteoric ice flowing off the continent that is interspersed with rifts that contain a thinner, mechanically weaker mixture that is largely sea ice.

As the rift system is advected towards the ice front over many decades, the rifts evolve under

the stress regimes through which they pass. In particular, the tensile stresses set up by shear between the fast-flowing SWIT and slower BIS cause failure and crack opening because the angle between the rifts, the grounding line and the flow direction of SWIT are optimal for the formation of maximum tensile stress (Humbert and Shuman, 2006). Sea ice thickness within the rifts varies: in some, it has a surface elevation of only a few meters. This suggests that it is relatively young (years to decades) and hence has a rheology relatively little altered by exposure to stress. This is in contrast to areas of older sea ice and much older blocks of ice that flowed from the land across the grounding line.

The margin of the relatively thin and slow-moving Brunt Ice Shelf is pinned by a small ice rise, the McDonald Ice Rumples. Between 1973 and 1985, this ice rise is known to have exerted an important control on the evolution of the ice front position (Simmons, 1986). Doake (2000) showed that the interaction between the ice rumples and the ice shelf is complex, however. Investigation of the crack propagation near their western end showed that the local and regional strain rates vary strongly across this area.

The BIS is known to have undergone marked changes in the recent past (Simmons and Rouse, 1984b,a; Gray and Short, 2001), and there is evidence of continuing changes in its flow (Gudmundsson, pers. comm.). The best-documented are the flow rates around Halley station, which has occupied several locations to the west of the McDonald Ice Rumples (75.52°S, 27.00°W in 1983). Halley has been relocated five times and is continually advected along a flowline, hence some change in the record of station flow rate can be expected even in an unchanging ice shelf flow regime. Several measurements from 1957 to 1968 are, however, in good agreement that this part of the BIS was flowing at an average of approximately 400 $\mathrm{m\,a^{-1}}$(Thomas, 1973). Between December 1968 and December 1969, flow at Halley accelerated by 10%, and by mid 1970, it had increased by 35%, accompanied by increased horizontal strain in the shelf 60 km up-flow Thomas (1973). One measurement from 1971 shows a slowdown back to 1969 rates (Thomas, 1973), but (Simmons and Rouse, 1984b) measured a 1968 to 1972 average of $431\pm22\,\mathrm{m\,a^{-1}}$, increasing to $740\pm9\,\mathrm{m\,a^{-1}}$from 1972 to 1982. This high velocity was maintained until 1999, when a pronounced deceleration began, and the current flow rate is around 530 $\mathrm{m\,a^{-1}}$(Gudmundsson, pers. comm.).

The changes described above cannot be explained solely as due to the changing location of Halley station. Three possible explanations have been suggested Simmons and Rouse (1984b): 1) A substantial calving event immediately east of the grounded McDonald Ice Rumples began in December 1968 when the ice backing up behind the rumples failed under longitudinal stress. A crack propagated rapidly eastwards (4 km in 10 days), and by January 1970, had formed a 100 m wide rift some 50 km long. In September 1971, an approximately 30 km-long berg detached from the shelf. Thomas (1973) argued that the rift formation and calving relieved up-stream stress, partially decoupling the shelf and ice rise and allowing the shelf to slide more rapidly past the grounded ice. This could explain the acceleration of Halley that, at the time, was only 10 km to the west. 2) The SWIT flow may have accelerated at the same time as the Brunt. Thomas (1973) measured flow along the eastern margin of the SWIT as 1300 $\mathrm{m\,a^{-1}}$in the late 1960s. Orheim (1986) reported a frontal advance rate of up to 4000 $\mathrm{m\,a^{-1}}$for 1973 to 1977, and from 1983 to 1984 the front advanced at up to 5300 $\mathrm{m\,a^{-1}}$Lange and Kohnen (1985), while Gray and Short (2001) measured SWIT surface flow rates of approximately 1500 $\mathrm{m\,a^{-1}}$in 1997. Though they are unsubstantiated by reliable, repeated measurements of flow rate at the same locations, these observations may suggest considerable changes in flow of the SWIT, and Simmons and Rouse (1984b) argue that such changes could have driven changes on the BIS. 3) The coupling of the faster SWIT flow with the slower BIS through the heterogeneous shear zone may vary. In this zone there is much new sea ice formed when the shelf fractures and open water is exposed. The sea ice rarely exceeds 50 m in thickness and these sea-ice filled chasms remain as zones of weakness in the shelf Thomas (1973). Open water is at times visible in satellite images of the chasms (Gray and Short (2001) and this study)

and major fractures have been observed to propagate through this weakly consolidated shear zone. Gray and Short (2001) argues that the McDonald Ice Rumples affect flow of the BIS only for a few kilometres up-flow, and that changes in flow at Halley may instead be due to changes in dynamics caused by a large fracture that has been propagating from the front into the shear zone, as well as fractures opening near the shelf grounding line. Conversely, Simmons and Rouse (1984b) argue that increased coupling of the BIS and SWIT through thickening of the shelf in the shear zone could explain the Halley acceleration, as they observed no open water on a visit to the area in 1981-1982.

It is clear from the above that the dynamics of the BIS-SWIT system are affected to some extent by the presence of mechanically weak, sea-ice filled rifts, and also by interaction with ice rises. The changes in flow described suggest a complex response to dynamic forcing that make this shelf of particular interest for a modelling study. In this study, we aim to examine the controls on ice shelf dynamics by developing a numerical model constrained by detailed measurements of ice thickness and flow.

3 The ice shelf thickness distribution

The flow of ice shelves is known to be very sensitive to ice thickness (Humbert et al., 2005; Humbert, 2005). To investigate this, numerical simulations therefore require estimates of ice thickness with a high spatial resolution.

In our study area, the Soviet Antarctic Expedition (SAE) performed an airborne Radio Echo Sounding (RES) survey in austral summer 1988/89 that obtained 48 tracks along Coats Land covering the BIS-SWIT and the Riiser-Larsen Ice Shelf. At that time, the area of sea ice and rifts that we see today was made up of ice 200 m thick (see Fig. 2, x=-600 km, y=1450 km). Since the glaciological regime at that time was considerably different from today, this dataset is not taken into account.

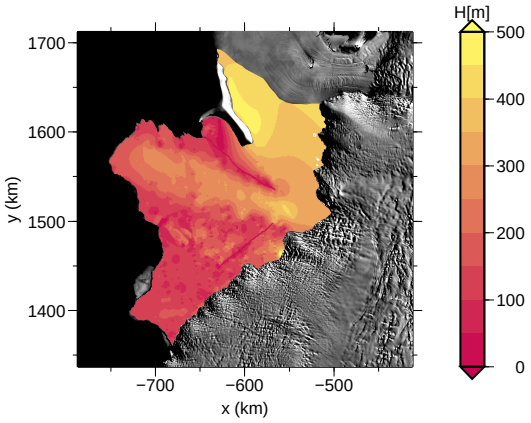

Figure 2: Ice thickness distribution as derived from RES data and ICESat GLAS surface elevation data trasformed to ice thickness assuming hydrostatic equilibrium, derived by using the technique of regional inter- and extrapolation.

In the southern part of the BIS-SWIT the Alfred Wegener Institute performed an airborne RES survey in 1994/95. Further ice thickness measurements were carried out by means of airborne RES by the British Antarctic Survey in 1996/97 in the area of the BIS only, and these were used to derive an ice thickness grid. These datasets combined cover only about 50% of the area, however, so to make a dataset covering the whole modelling domain, we used new ice surface elevation data to calculate ice thickness. Surface elevation data from the NASA laser-altimeter satellite, ICESat, from 2003 cover the modelling domain with numerous tracks and thus allows us to derive the spatial distribution of the ice thickness with high precision. We calculated the ice thickness under the assumption of hydrostatic equilibrium and the density profile of Schytt (1958) for meteoric ice with a thickness larger than 20 m, and a relation between sea ice draft and ice thickness from Ackely et al. (1990); Eicken et al. (1994) for ice thinner than 20 m. We interpolated thickness between tracks taking into account features (e.g. icebergs, sea ice floes) detected manually in satellite imaginary (after Humbert and Shuman, 2006). This resulted in single tiles, which we then combined together to form a complete ice thickness grid of the area (Fig. 2).

4 The present ice shelf velocity field

To measure the surface flow field of the BIS, we employed automated feature tracking with synthetic aperture radar (SAR) satellite images acquired by the European Space Agency's ENVISAT platform. SAR feature tracking has frequently been used to measure glacier flow because such active SAR systems operating at microwave frequencies are independent of solar illumination and cloud cover, and are sensitive to gross glacier surface features and subtle variations in snow properties (e.g. Strozzi et al., 2002; Pritchard and Vaughan, 2005).

The offset of features such as crevasses tracked between pairs of satellite images is made up of contributions from slight differences in satellite position during image acquisition and ice-movement between the acquisition times. These contributions must be separated in order to isolate glacier or ice-shelf movement. Typically, the satellite orbital tracks are known only to an uncertainty of tens of metres, and this translates directly into systematic error in the estimate of the flow component for a given feature. Consequently, the orbital component of the offset is often refined using multiple static (zero flow) rock areas within the scene as reference points (Pritchard et al., 2005). Alternatively, Scambos et al. (1992) showed that large-scale surface flow features tied to glacier bed topography (icefalls and similar) can be used for this purpose. In the case of the BIS and many of Antarctica's outlet glaciers and ice shelves, however, no rock outcrops are present and the ice shelves have no flow features tied to bed topography, so this refinement process cannot be followed.

For this study, we made use of the high quality of orbital knowledge of the ENVISAT platform. This is the result of advanced on-board orbit-tracking technology, a notable improvement over previous SAR systems (Doornbos and Scharroo, 2005) that removes the need for rock areas within the tracking scene. We coregistered a 35-day-interval pair of Single Look Complex (SLC) SAR images from May 12th and June 16th 2005 using only the ENVISAT orbit state vectors, refined by the Delft Institute for Earth-oriented Space Research, in combination with the RAMP digital elevation model (Liu et al., 1999). This removed the orbital component of the image offset, including any topographic contribution resulting from viewing the scene from differing positions. We then tracked the movement of features within the scene over the 35-day period using Gamma software and the method of Pritchard and Vaughan (2005) to produce surface flow vectors of the BIS and adjacent Caird Coast at a spacing of 100 m. We filtered these vectors for outliers to remove false-match tracking offsets, smoothed them with a linear-distance-weighted averaging kernel and then geocoded to give a product with spacing of 1000 m (Fig. 3). Using a tidal model (Padman et al., 2002), we calculated the tidal displacement between the scenes and found that the tidal contribution to the overall measured shelf movement was negligible.

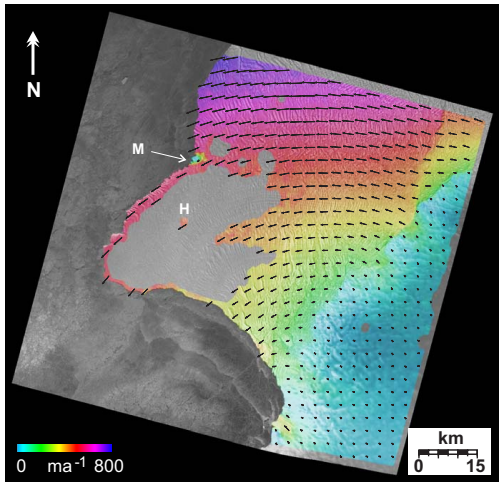

Figure 3: The flow field of the Brunt Ice Shelf measured using SAR feature-tracking (in colour and vector arrows), overlayed on a background greyscale SAR image. Flow was verified at Halley (H) and and the McDonald Ice Rumples (M).

We assessed the accuracy of the flow field over the McDonald Ice Rumples, which we presume to be nearly static, and at Halley Station where continuous GPS measurements are available. Over the 35-day tracking period, the GPS at Halley showed that the station moved 50.24 m, a mean flow of 529 ma^{-1}. The feature tracking for the sample of points in the area surrounding Halley (a 165-sample subset of the patch marked H in Fig. 3) produced a mean of 49.98 m, or 522 ma^{-1}(standard

deviation, after filtering, of 3.65 ma^{-1}). The easting component was measured as 464 $\mathrm{ma}^{-1}$by GPS and 449 $\mathrm{ma}^{-1}$by tracking, and the northing as 256 $\mathrm{ma}^{-1}$by GPS, -266 $\mathrm{ma}^{-1}$by tracking. Over the McDonald Ice Rumples (M in Fig. 3), the tracking indicates a slight flow trend with magnitude of 26 ma^{-1}in a westerly direction. Given the small size of the inaccuracy (0.5% in magnitude at Halley) and the shortage of points where flow can be verified, we did not attempt to calculate a correcting polynomial for the flow field.

5 The model

A three-dimensional, thermodynamically consistent dynamic model for ice shelf flow was developed by Weis (2001), using a general, continuum mechanical approach. Here, we solve diagnostically the elliptic boundary-value problem for the horizontal velocity in the shallow-shelf approximation (SSA). The deformation of ice is described by Glen's flow law (e.g. Paterson, 1994),

$$\boldsymbol{D} = EA(T)f(\sigma)\,\boldsymbol{t}^{\mathrm{D}}, \quad \text{with } f(\sigma) = \sigma^{n-1},\ n = 3, \tag{1}$$

where $\boldsymbol{D} = \operatorname{sym}\operatorname{grad}\boldsymbol{v}$ is the strain-rate tensor [symmetric part of the gradient of the velocity $\boldsymbol{v} = (v_x, v_y, v_z)$], $\boldsymbol{t}^{\mathrm{D}}$ the Cauchy stress deviator, $\sigma = [\mathrm{tr}\,(\boldsymbol{t}^{\mathrm{D}})^2/2]^{1/2}$ the effective stress, n the stress exponent, T the absolute temperature, $A(T)$ the flow-rate factor (see below) and E the flow enhancement factor.

Insertion of the flow law (1) in the SSA limit of the horizontal force balance yields the elliptic differential equations for the horizontal velocity (v_x, v_y) (see Weis et al., 1999),

$$\begin{aligned}
2\frac{\partial}{\partial x}\left(\bar{\nu}\frac{\partial v_x}{\partial x}\right) + \frac{\partial}{\partial x}\left(\bar{\nu}\frac{\partial v_y}{\partial y}\right) + \frac{1}{2}\frac{\partial}{\partial y}\left[\bar{\nu}\left(\frac{\partial v_x}{\partial y} + \frac{\partial v_y}{\partial x}\right)\right] &= \varrho H\frac{\partial H}{\partial x} + \frac{\tau_x^{\mathrm{d}}}{\rho g},\\
\frac{\partial}{\partial y}\left(\bar{\nu}\frac{\partial v_x}{\partial x}\right) + 2\frac{\partial}{\partial y}\left(\bar{\nu}\frac{\partial v_y}{\partial y}\right) + \frac{1}{2}\frac{\partial}{\partial x}\left[\bar{\nu}\left(\frac{\partial v_x}{\partial y} + \frac{\partial v_y}{\partial x}\right)\right] &= \varrho H\frac{\partial H}{\partial y} + \frac{\tau_y^{\mathrm{d}}}{\rho g},
\end{aligned} \tag{2}$$

where the coordinates x and y span the horizontal plane, $\bar{\nu}$ is the effective viscosity, $\varrho = (\rho_{\mathrm{sw}} - \rho)/\rho_{\mathrm{sw}}$ the relative density (ρ_{SW}: density of sea water (1028 $\mathrm{kg\,m}^{-3}$), ρ_{ice}: density of meteoric ice (910 $\mathrm{kg\,m}^{-3}$)), H the ice thickness, g the gravity acceleration (9.81m s^{-2}), and $\tau_{x,y}^{\mathrm{d}}$ the basal drag in the x and y directions. The latter is set to zero for the floating ice shelf, but can be assigned non-vanishing values for grounded ice rumples (not done in this study). For the effective viscosity,

$$\bar{\nu} = \frac{1}{\rho g} d^{\frac{1-n}{n}} \int_{h_{\mathrm{b}}}^{h_{\mathrm{s}}} E_{\mathrm{s}} B(T)\, dz, \tag{3}$$

where z is positive upward, $E_{\mathrm{s}} = E^{-1/n}$ is the stress enhancement factor, $B(T) = [A(T)]^{-1/n}$ the associated rate factor, h_{s} and h_{b} are the positions of the free surface and the base (ice-ocean interface), respectively (ice thickness $H = h_{\mathrm{s}} - h_{\mathrm{b}}$), and

$$d = \sqrt{\left(\frac{\partial v_x}{\partial x}\right)^2 + \left(\frac{\partial v_y}{\partial y}\right)^2 + \frac{\partial v_x}{\partial x}\frac{\partial v_y}{\partial y} + \frac{1}{4}\left(\frac{\partial v_x}{\partial y} + \frac{\partial v_y}{\partial x}\right)^2} \tag{4}$$

is the effective strain rate (second invariant of the strain-rate tensor). For the associated rate factor $B(T)$, the relation by Hooke (1981) is employed,

$$B(T) = B_0 \exp\left(\frac{T_0}{T} - \frac{C}{(T_{\mathrm{r}} - T)^k}\right), \tag{5}$$

with the parameters $B_0 = 6.984 \times 10^{-6}\,\mathrm{kPa\,s^{1/3}}$, $T_0 = 3155\,\mathrm{K}$, $T_\mathrm{r} = 273.39\,\mathrm{K}$, $k = 1.17$ and $C = 0.16612\,\mathrm{K}^k$.

The elliptic system of differential equations (2) is subject to two different types of boundary conditions: (i) inflow of ice along the grounding line from the adjacent inland ice, and (ii) a vertically integrated stress boundary condition at the front edge. Further, the ice-thickness distribution $H(x, y)$ and the temperature field $T(x, y, z)$ must be prescribed.

The equations are solved using the commercial software COMSOL using the finite element (FE) technique. COMSOL is a high performance FE solver for stationary and non-stationary nonlinear systems with an optimized user interface.

6 Simulation set-up: input quantities

The model described above requires the following input quantities:

- Position of the grounding line(s) and calving front.
- Inflow velocities.
- Ice thickness.

Since there is no information about the vertical ice temperature profile, neither direct information as a measured temperature profile, nor indirect information as measured bottom melting or properties of an ice core, we assumed the flow rate factor B (see Eq. 5) to be constant. We determined the value for $B \cdot E_\mathrm{s}$ by comparison with measured flow speeds as described below (Section 7).

6.1 Modelling domain

The modelling domain covers the Brunt Ice Shelf and the Stancomb-Wills Ice Tongue. We defined the northern margin from the ice front north of Bakewell Island in an arch along visible flow lines on the Riiser-Larsen Ice Shelf to the grounding line at Princess Martha Coast. The area is shown in Fig. 1. There are two major ice rises, Lyddan Island (74.25°S S, 20.45°S W) and the McDonald Ice Rumples (75.47°S, 26.30°W) and three nameless tiny ice rises in the northern part of the domain, close to the grounding line.

6.2 Inflow velocities and ice thickness

We used the following inflow velocities: along the grounding line of the BIS from image cross-correlation data measured in 2005 (Section 4); in the intermediate area between BIS and SWIT and along the grounding line of the SWIT from InSAR data from 2001 (Laurence Gray, pers. comm.); along the grounding line of the ice rises the velocity was assumed to be zero (after Sanderson (1979)). For ice thickness, we used the field covering the model domain described in Section 3.

7 Reference Simulation

The settings described above (Section 6) define the reference simulation that we call REF. The product of stress enhancement factor and flow rate factor $B \cdot E_\mathrm{s}$ is chosen such that the absolute value of the mean difference between measured (v_measured) and simulated (v_REF) speeds is minimized,

$$\left| \frac{1}{N} \sum_{n=1}^{N} (v_{\mathrm{measured},n} - v_{\mathrm{REF},n}) \right| \stackrel{!}{=} \min, \tag{6}$$

where the index n numbers the N measured velocity points at a distance of at most 500 m from the finite element node. This procedure yields the factor $B \cdot E_s = 0.92e^8\,\mathrm{Pas}^{1/3}$(corresponding to the flow rate factor times a flow enhancement factor $A \cdot E = 1.28\,(\mathrm{kPa})^{-3}\mathrm{s}^{-1}$), for which the remaining mean difference is $+35.3\,\mathrm{ma}^{-1}$.

Figure 4 shows the horizontal velocities of the reference simulation and a scatter plot of the measured and simulated speed.

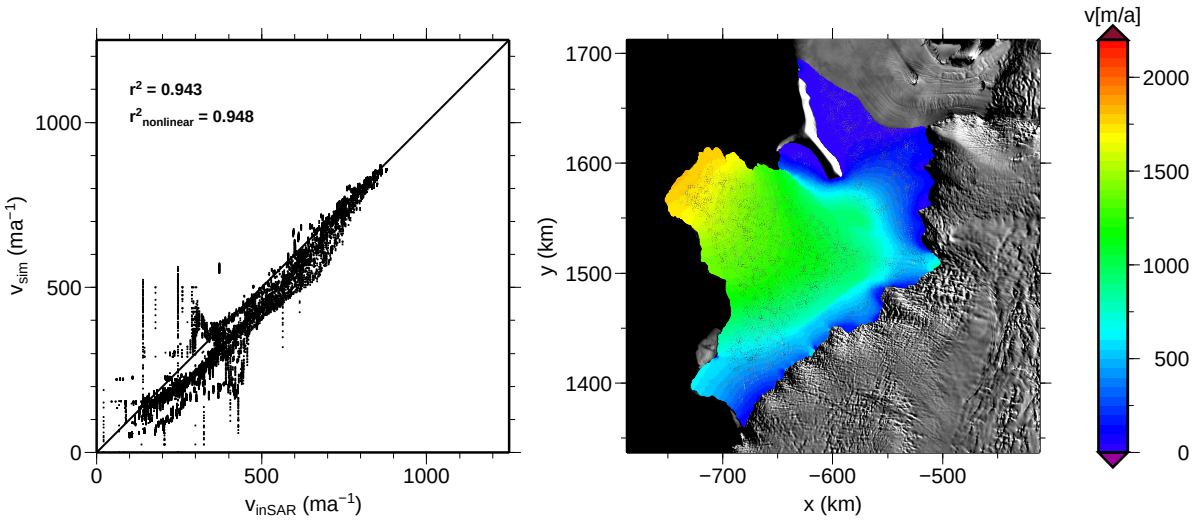

Figure 4: Reference Simulation. Left: Scatter plot of the measured velocities vs. the simulated velocities. Right: Simulated speed distribution for the BIS-SWIT.

Note that the measured flow dataset used here for comparison covers the BIS only and thus a comparison of the simulated speeds of the SWIT is not included. Since the speed of the BIS decreased in the five years between 2001 and 2006 in parts by up to $200\,\mathrm{ma}^{-1}$it is not reasonable to use the InSAR dataset that covers the SWIT and the cross-correlation dataset that covers the BIS at the same time. Furthermore, the ice thickness dataset derived from ice surface elevation achieved in 2003 and later represent the glaciological regime of 2006 rather than the one in 2001.

8 Varied ice properties

As shown in Section 5, the effective viscosity is a function of the flow rate factor and the enhancement factor. Both quantities represent the mechanical properties of ice and determine if the ice is stiff or soft. The rate factor parameterises the temperature and water content dependence, whereas the enhancement factor is still a quantity that is used to parameterise every effect beyond temperature and water content. These effects include stress history, grain size, anisotropy, inclusions etc. Ice in shear zones has undergone damaging and thus the mechanical properties are believed to be substantially different from ordinary meteoric polycrystalline ice shelf ice.

A previous modelling study of the BIS-SWIT system that did not employ cartesian coordinates Hulbe (2005) included in the first term of the right hand side of Eq. 2 the product of ice thickness times ice surface elevation gradient. Very precise spatial ice surface elevation and thickness distributions were required, and the flotation criteria used for the computation of the ice thickness was adjusted in the sea ice zones to the flotation criteria of sea ice. The advantage of the modelling approach used in this study over that of Hulbe (2005) is that only the spatial distribution of the ice thickness distribution is required and the model is not prone to inconsistencies between ice thickness and ice surface elevation. The high quality ice thickness distribution we use here means that we do not need to make the flotation-criteria adjustments for sea ice that were previously

necessary Hulbe (2005).

The position of two rifts in the BIS-SWIT systen were detected manually from the MOA image. The extent of the rift between Lyddan Island and SWIT was defined by using a combination of visible imaginary and ICESat surface elevation data. The rift appears in the ICESat data as a jump in the surface elevation. Closer to the grounding line the jump disappears and the ice surface topography on both sides are similar. This marks the position of the end of the rift. A second rift, situated in the sea ice zone, was incorporated in the numerical simulations. This rift is formed from release of tensile stress between the fast flowing SWIT and the slow moving BIS. ICESat surface elevation data shows a low elevation across the whole path visible in the MOA image. The location of the rifts are visible in Fig. 2 since they have very low ice thickness. The material properties of the rifts are assumed to be different from the surrounding meteoric or sea ice, as the ice in the rift has undergone damaging and is thus expected to be less stiff than non-damaged ice. Therefore, the flow rate factor $B \cdot E_\mathrm{s}$ was reduced. Simulations with $B \cdot E_\mathrm{s} = 0.3{\cdot}10^8$, $0.4{\cdot}10^8$, $0.5{\cdot}10^8$, $0.6{\cdot}10^8$, $0.7{\cdot}10^8$ and $0.8{\cdot}10^8\,\mathrm{Pas}^{1/3}$inside the rift were carried out. The results are shown in Fig. 5.

The left panel of the figure shows the result obtained using $B \cdot E_\mathrm{s} = 0.4 \cdot 10^8\,\mathrm{Pas}^{1/3}$, which corresponds to the softest parameter settings. The velocity difference across the rift is increased compared to the reference simulation. The rift between Lyddan Island and SWIT leads to a decrease of the low velocities on the side of Lyddan Island, whereas the velocities on the side of SWIT is increasing. The right panel of Fig. 5 shows a scatter plot in which the simulated speeds with varied rift properties is drawn versus the reference simulation. Each dot represents one node in the finite element mesh. The colour denote the parameters $B \cdot E_\mathrm{s}$= $0.3{\cdot}10^8$, $0.4{\cdot}10^8$, $0.5{\cdot}10^8$, $0.6{\cdot}10^8$, $0.7{\cdot}10^8$ and $0.8{\cdot}10^8\,\mathrm{Pas}^{1/3}$. The figure shows that in all parameter settings, the velocity of the slow-flowing areas from the rift towards Riiser-Larsen Ice Shelf decrease, whereas higher velocities, arising from SWIT, increase by the softening of the rift. This approach is however limited, since the ice moving from Riiser-Larsen Ice Shelf across the rift, located around x=-670 km and y=1570 km, experience a stagnation from the weaking of the rift properties.

The rift in the sea ice area shows in general the same decoupling behaviour. The velocities between the grounding line and the rift decrease. Velocities on the other side of the rift are increasing. This rift has also an effect on the direction of the ice movement. The ice between the rift and the ice front is turning even more westward. Ice coming from the inflow across the grounding line along Coats Land is experiencing a westward turn, too.

The rheology of sea ice deformation is very likely not following Glen's flow law, since the mechanical properties of sea ice are considerably different from meteoric ice. On the other hand, InSAR and feature tracking velocities show that there are no discontinuities in the flow field, so that the sea ice is deforming with the surrounding meteoric ice. Therefore, we consider that Glen's flow law can be applied to sea ice ares as well, using flow rate factors that are remarkably different from meteoric ice.

The sea ice areas were detected manually and the flow rate factor $B \cdot E_\mathrm{s}$ inside these areas were set to $0.3{\cdot}10^8$, $0.4{\cdot}10^8$, $0.5{\cdot}10^8$, $0.6{\cdot}10^8$, $0.7{\cdot}10^8$ and $0.8{\cdot}10^8\,\mathrm{Pas}^{1/3}$. The resulting flow field for $B \cdot E_\mathrm{s} = 0.4 \cdot 10^8\,\mathrm{Pas}^{1/3}$is shown in Fig. 6 (left panel). The effect of the weakening of the sea ice is strongest on the western corner of SWIT, which in the simulation accelerated by up to $1922\,\mathrm{ma}^{-1}$that is 6% faster than the reference simulation. The BIS is in general not affected as much as the SWIT by the softening of the sea ice zones, in particular in the south-western part of the BIS the velocity field is almost unchanged.

The right panel of Fig. 6 displays a scatter plot of the simulated velocities with softer sea ice versus the reference simulation. Each dot represents one node in the finite element mesh and the colour denotes different values for the flow rate factor. It is apparent that the different parameter settings affect areas with velocities from $\sim$$750\,\mathrm{ma}^{-1}$much more than slower flowing areas. The higher velocities are all situated in the SWIT area. The sea ice zone is acting as a sideward bound

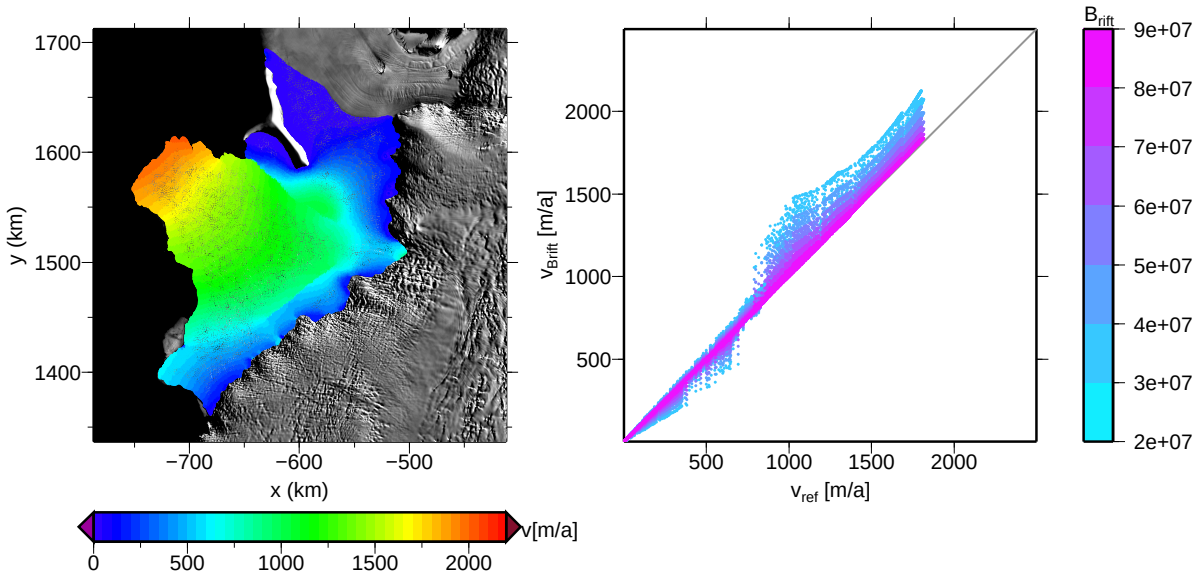

Figure 5: Varied rift properties. Left panel: Simulated flow field for $B \cdot E_s = 0.4e^8\,\mathrm{Pas}^{1/3}$inside the rifts. Right panel: Scatter plot of the simulated velocities with softer sea ice versus the reference simulation. Each dot represents one node in the finite element mesh. The colour denote the parameters $B \cdot E_s$= $0.3{\cdot}10^8$, $0.4{\cdot}10^8$, $0.5{\cdot}10^8$, $0.6{\cdot}10^8$, $0.7{\cdot}10^8$ and $0.8{\cdot}10^8\,\mathrm{Pas}^{1/3}$.

on the SWIT and as this zone is weakened the tensile stress acting between the fast flowing SWIT and the slow flowing BIS decreases. The decoupling between the dynamical regimes thus becomes stronger as the sea ice is weakened.

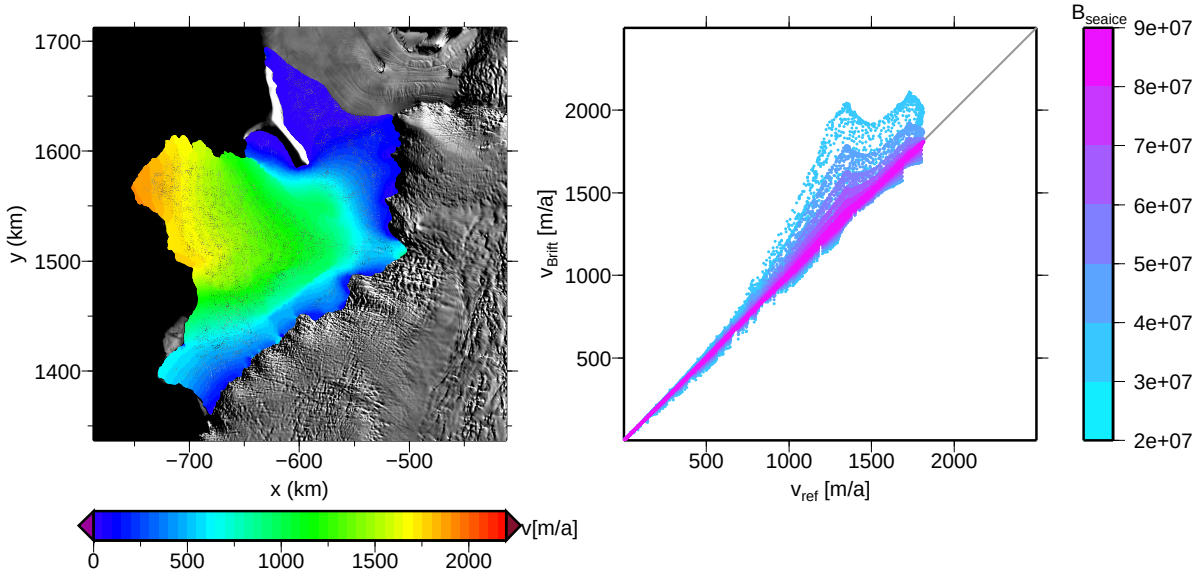

Figure 6: Varied sea ice properties. Left panel: Simulated flow field for $B \cdot E_s = 0.4 \cdot 10^8\,\mathrm{Pas}^{1/3}$inside the sea ice areas. Right panel: Scatter plot of the simulated velocities with softer sea ice versus the reference simulation. Each dot represents one node in the finite element mesh. The colour denote the parameters $B \cdot E_s$= $0.3{\cdot}10^8$, $0.4{\cdot}10^8$, $0.5{\cdot}10^8$, $0.6{\cdot}10^8$, $0.7{\cdot}10^8$ and $0.8{\cdot}10^8\,\mathrm{Pas}^{1/3}$.

The studies discussed in this section show that the incorporation of local structures like rifts

and other weak zones affect the flow field strongly. A measured velocity field that covers the whole modelling domain would enable us to determine the flow rate parameters in the different structures, which would greatly improve our understanding of weak and damaged zones.

9 What happens if the sea ice disappears?

As described in Section 2, the sea ice between BIS and SWIT was not always present. That leads us to the question of how the ice flow of the BIS- SWIT system changes if the sea ice disappears. The margin location when sea ice was absent was manually mapped from MOA images and is shown in Fig. 7 (left panel). The inflow along the grounding line is unchanged, whereas the new boundaries are assigned with ice front boundary conditions.

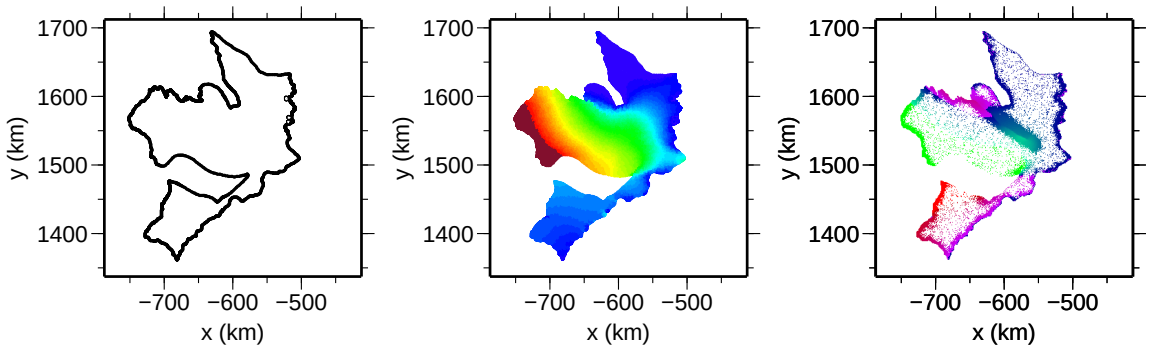

Figure 7: Left: Boundaries without sea ice. Middle: Horizontal velocity field without sea ice and parameters settings of the reference simulation. Right: Difference between the reference simulation and the simulation without sea ice.

The resulting horizontal velocity distribution is shown in Fig. 7 (middle panel). The velocities along the ice front of SWIT increase dramatically, reaching velocities as high as $2600\,\mathrm{ma}^{-1}$, whereas the reference setup showed a maximum speed at the ice front of $1800\,\mathrm{ma}^{-1}$. Although the speeds of the ice front shown by Orheim (1986) are not matched by the model with this setup, the pattern is correct.

A change in the ice properties along the rift between SWIT and Lyddan Island does not influence the maximum speed along the ice front, since the highest speeds arise at the western corner of the SWIT, however, the varied ice properties along the rift do affect the speeds at the eastern side of the SWIT, as discussed in Section 8.

Figure 7 (right panel) shows the difference of the flow field without sea ice to the reference simulation. It is apparent that in absence of sea ice, SWIT flows faster, whereas BIS slows. Therefore, the observation of deceleration of the BIS, discussed in Section 2, could be a hint of a change in the dynamics of the sea ice and iceberg zone.

10 Conclusions

We were able to define $B \cdot E_\mathrm{s}$, such that the difference between the simulated velocities and the measured velocities discussed in Section 4 was minimized and the correlation factor is as high as 0.943.

In Section 8 we carried out studies in which we changed ice properties inside rifts of the BIS-SWIT and the sea ice. We can conclude, that the incorporation of local features lead to an overall improvement of the numerical simulations. Softer ice inside the rifts lead to decoupling of the ice speeds on both sides of the rift and thus, ice in slow moving areas are decelerating and ice in

fast moving areas is accelerating. Softening of the sea ice leads to an increase in speeds along the western ice front of SWIT and thus boost a decoupling between the fast flowing SWIT and the slow moving BIS. The south-western part of the BIS is not affected by changing sea ice properties.

Thomas (1973) observed open water between the icebergs in the area between SWIT and BIS, which gave us the motivation to performing simulations in which the sea ice area was inexisting. The simulations show, that the speeds along the western side of the ice front of SWIT are increasing dramatically. This is in agreement with the observed high speeds of Orheim (1986). The resulting difference of the flow field to the reference simulation show that in absence of sea ice, the velocities of SWIT are increasing, whereas BIS is decelerating. Therefore, the observation of deceleration of the BIS could be a hint of a change in the dynamics of the sea ice and iceberg zone.

It would be very valuable to extent the feature tracking velocities over the whole modelling domain in order to obtain data that is acquired at the same time over the whole ice shelf and, furthermore, that is acquired at the same time as the surface elevation data that is used to derive the ice thickness.

11 Acknowledgements

A. Humbert was supported by the German Research Foundation (Deutsche Forschungsgemeinschaft, DFG) under grant no. HU 412/39-4. ENVISat data were supplied by the European Space Agency.

References

Ackely, S. F., M. A. Lange, and P. Wadhams [1990]. Snow cover effects of Antarctic sea ice thickness. *CRREL Monographs*, **90**(1):16–21.

Doake, C. S. M. [2000]. Recent glaciological investigations on Brunt Ice Shelf. *Filchner-Rønne Ice Shelf Programme (FRISP), Report*, **13**:13–18.

Doake, C. S. M., H. F. J. Corr, H. Rott, P. Skvarca, and N. W. Young [1998]. Breakup and conditions for stability of the northern Larsen Ice Shelf, Antarctica. *Nature*, **391**:778–780.

Doake, C. S. M. and D. G. Vaughan [1991]. Rapid disintegration of the Wordie Ice Shelf in response to atmospheric warming. *Nature*, **350**(6316):328–330.

Doornbos, E. and R. Scharroo [2005]. Improved ERS and ENVISAT Precise Orbit Determination. *Proc. of the Envisat and ERS Symposium, Salzburg, Austria 6-10 September 2004*, **ESA SP-572**.

Eicken, H., H. Oerter, H. Miller, W. Graf, and S. Kipfstuhl [1994]. Textural characteristics and impurity content of meteoric and marine ice in the Ronne Ice Shelf. *Journal of Glaciology*, **40**(135):386–398.

Gray, L. and N. Short [2001]. Dynamics of the Stancomb-Wills Glacier tongue and the Brunt Ice Shelf. *unpublished report*, Seiten 1–19.

Hooke, R. L. [1981]. Flow Law for Polycrystalline Ice in Glaciers: Comparison of Therretical Predictions, Laboratory Data, and Field Measurements. *Reviews of Geophysics and Space Physics*, **19**(4):664–672.

Hulbe, C. L. [2005]. Marine Ice Modification of Fringing Ice Shelf Flow. *Arctic, Antarctic and Alpine Research*, **37**(3):323–330.

Humbert, A. [2005]. *Simulations of the Flow of the Ross Ice Shelf, Antarctica: parameter sensitivity tests and temperature-dependent ratefactor*. Department of Mechanics, Darmstadt University of Technology. ISBN 3-945868-10-3.

Humbert, A., R. Greve, and K. Hutter [2005]. Parameter sensitivity studies for the ice flow of the Ross Ice Shelf, Antarctica. *Journal of Geophysical Research, in print*, **110(F4)**(F04022):doi: 10.1029/2004JF000170.

Humbert, A. and C. A. Shuman [2006]. The Beauty and Complexity of the Brunt Ice Shelf from MOA and ICESat. *submitted to Journal of Glaciology*.

Lange, M. A. and H. Kohnen [1985]. Ice front fluctuations in the eastern and southern Weddell Sea. *Annals of Glaciology*, **6**:187–191.

Liu, H., K. Jezek, and B. Li [1999]. Development of Antarctic digital elevation model by integrating cartographic and remotely sensed data: A geographic information system based approach. *Journal of Geophysical Research*, **104**:23,199–23,213.

Orheim, O. [1986]. Flow and thickness of Riiser-Larsenisen, Antarctica. *Norsk Polarinstitutt Skrifter*, **187**:5–22.

Orsi, A. H., G. C. Johnson, and J. L. Bullister [1999]. Circulation, mixing, and production of Antarctic Bottom Water. *Progress in Oceanography*, **43**:55–109.

Padman, L., H. A. Fricker, R. Coleman, S. Howard, and L. Erofeeva [2002]. A new tide model for the Antarctic ice shelves and seas. *Annals of Glaciology*, **34**:247–254.

Paterson, W. S. B. [1994]. *The Physics of Glaciers*. Pergamon Press, Oxford, third Auflage.

Pritchard, H., T. Murray, A. Luckman, T. Strozzi, and S. Barr [2005]. Glacier surge dynamics of Sortebrae, East Greenland, from Synthetic Aperture Radar feature tracking. *Journal of Geophysical Research*, **110**(F3):doi:10.1029/JF000233.

Pritchard, H. D. and D. G. V. Vaughan [2005]. Widespread Acceleration of Tidewater Glaciers on the Antarctic Peninsula. *Submitted to JGR Earth Surface*.

Rignot, E., G. Casassa, P. Gogineni, W. Krabill, A. Rivera, and R. Thomas [2004]. Accelerated ice discharge from the Antarctic Peninsula following the collapse of Larsen B ice shelf. *Geophysical Research Letters*, **31**(L18401):doi:10.1029/2004GL020697.

Rignot, E., S. Casassa G. amd Gogineni, P. Kanagaratnam, W. Krabill, H. Pritchard, A. Rivera, R. Thomas, J. Turner, and D. Vaughan [2005]. Recent ice loss from the Fleming and other glaciers, Wordie Bay, West Antarctic Peninsula. *Geophysical Research Letters*, **32**(L07502):doi:10.1029/2004GL021947.

Rott, H., P. Skvarca, and T. Nagler [1996]. Rapid collapse of northern Larsen Ice Shelf, Antarctica. *Science*, **271**(5250):788–792.

Sanderson, T. J. O. [1979]. Equilibrium profile of ice shelves. *Journal of Glaciology*, **24**(90):435–459.

Scambos, T., J. Bohlander, C. Shuman, and P. Skvarca [2004]. Glacier acceleration and thinning after ice shelf collapse in the Larsen B embayment, Antarctica. *Geophysical Research Letters*, **31**(L18402):doi:10.1029/2004GL020670.

Scambos, T. A., R. A. Bindschadler, M. J. Dutkiewicz, and J. C. Wilson [1992]. Application of image cross-correlation to the measurement of glacier velocity using satellite image data. *Remote Sensing Environ.*, **42(3)**:177–186.

Schytt, V. [1958]. Glaciology.II. The inner structure of the ice shelf at Maudheim as shown by core drilling. *Norwegian-British-Swedish Antarctic Expedition 1949-52, Scientific Results*, **4,C**.

Simmons, D. A. [1986]. Flow of the Brunt Ice Shelf, Antarctica, derived from Landsat images, 1974-1985. *Journal of Glaciology*, **32**(111):252–254.

Simmons, D. A. and J. R. Rouse [1984a]. Accelerating flow of the Brunt Ice Shelf, Antarctica. *Journal of Glaciology*, **30**(106):377–380.

Simmons, D. A. and J. R. Rouse [1984b]. Geomagnetic measurements made on the moving ice shelf at Halley, Antarctica. *Geophysical Surveys*, **6**:407–417.

Strozzi, T., A. Luckman, T. Murray, U. Wegmuller, and C. L. Werner [2002]. Glacier motion estimation using SAR offset-tracking procedures. *IEEE TRANSACTIONS ON GEOSCIENCE AND REMOTE SENSING*, **40**(11):2384–2391.

Thomas, R. H. [1973]. The creep of ice shelves: theory. *Journal of Glaciology*, **12**(64):45–53.

Weis, M. [2001]. *Theory of shallow ice shelves and numerical implementation*. Dissertation, Institut für Mechanik AGIII, Technische Universität Darmstadt, Germany.

Weis, M., R. Greve, and K. Hutter [1999]. Theory of Shallow Ice Shelves. *Continuum Mechanics and Thermodynamics*, **11**:11–50.